manuscript t119611 for review

IUCrJ
ISSN 2052-2525

The crystal structure of the killer fibre erionite from Tuzköy (Cappadocia, Turkey)

Carlotta Giacobbe, Anna Moliterni, Dario Di Giuseppe, Daniele Malferrari, Jonathan P. Wright, Michele Mattioli, Simona Ranieri, Cinzia Giannini, Laura Fornasini, Enrico Mugnaioli, Paolo Ballirano and Alessandro F. Gualtieri

Category: *research papers*

Co-editor:

Telephone:

Fax:

Email:

Submitting author:

Carlotta Giacobbe

Structure of Materials, European Synchrotron Radiation FAcility, 71 avenue des Martyrs, GRENOBLE, 38000, France

Telephone: 0670434414

Fax: ?

Email: carlotta.giacobbe@gmail.com

The crystal structure of the killer fibre erionite from Tuzköy (Cappadocia, Turkey)

Carlotta Giacobbe[1]*, Anna Moliterni[3]*, Dario Di Giuseppe[2], Daniele Malferrari[2], Jonathan P. Wright[1], Michele Mattioli[4], Simona Raneri[5], Cinzia Giannini[3], Laura Fornasini[5], Enrico Mugnaioli[6], Paolo Ballirano[7], Alessandro F. Gualtieri[2]

[1]European Synchrotron Radiation Facility, Avenue des Martyrs 71, 38040 Grenoble, France
[2]Dipartimento di Scienze Chimiche e Geologiche, Università degli Studi di Modena e Reggio Emilia, Via G. Campi 103, 41125 Modena, Italy
[3]Institute of Crystallography-CNR, Via Amendola 122/o, 70126 Bari, Italy
[4]Dipartimento di Scienze Pure ed Applicate, Università degli Studi di Urbino Carlo Bo, Campus Scientifico Enrico Mattei, 61029 Urbino, Italy
[5]ICCOM-CNR, Institute of Chemistry of Organometallic Compounds, Italian National Research Council, Via G. Moruzzi 1, 56124, Pisa, Italy
[6]Dipartimento di Scienze della Terra, Università di Pisa, Via S. Maria 53, Pisa 56126, Italy
[7]Dipartimento di Scienze della Terra, La Sapienza Università di Roma, Piazzale Aldo Moro 5, 00185, Roma, Italy

*E-mail: carlotta.giacobbe@esrf.fr, annagrazia.moliterni@ic.cnr.it

Synopsis

Synchrotron nano-diffraction coupled with electron diffraction and spectroscopic techniques revealed the crystal structure of zeolite erionite from Cappadocia. These results will fill in the gap for a precise modeling of the carcinogenicity of this killer fibre.

Abstract

Erionite is a non-asbestos fibrous zeolite classified by the International Agency for Research on Cancer (IARC) as a Group 1 carcinogen and is considered today similar or even more carcinogenic than the six regulated asbestos minerals. Exposure to fibrous erionite has been unequivocally linked to cases of malignant mesothelioma (MM) and this killer fibre is assumed to be directly responsible for more than 50% of all deaths in the population of the villages of Karain and Tuzköy in central Anatolia (Turkey). Erionite usually occurs in bundles of thin fibres and very rarely as single acicular or needle-like fibres. For this reason, a crystal structure of this fibre has not been attempted to date although an accurate characterization of its crystal structure is of paramount importance for the understanding of its toxicity/carcinogenicity potential.

In this work, we report on a combined approach of microscopic (SEM, TEM, electron diffraction), spectroscopic (micro-Raman), and chemical techniques with synchrotron nano-single crystal diffraction that allowed to obtain the first reliable *ab-initio* crystal structure of this killer zeolite. The refined structure showed regular T−O distances (in the range 1.61−1.65 Å) and extra-framework content in line with the chemical formula $(K_{2.63}Ca_{1.57}Mg_{0.76}Na_{0.13}Ba_{0.01})[Si_{28.62}\ Al_{7.35}]O_{72}\cdot 28.30H_2O$.

The synchrotron nano-diffraction data combined with three dimensional-electron diffraction (3DED), allowed us to unequivocally rule out the presence of offretite. These results are of paramount importance for understanding the mechanisms by which erionite induces toxic damage and confirming the physical similarities with asbestos fibres.

Keywords:

Erionite, nano-diffraction, asbestos, *ab-initio* structure solution, mesothelioma

1. Introduction

Erionite is a natural zeolite that belongs to the ABC-6 family (Gottardi & Galli, 1985). Its periodic building unit (PerBU) consists of a hexagonal array of planar 6-membered rings of (Si, Al)O_4 tetrahedra (T6-rings) related by pure translations along *a* and *b* (Van Koningsveld, 2007). Erionite (ERI) has average formula $K_2(Ca_{0.5},Na)_7[Al_9Si_{27}O_{72}]\cdot 28H_2O$ (Passaglia & Sheppard, 2001) and hexagonal symmetry with space group $P6_3/mmc$ and unit-cell parameters $a \sim 13.15$ Å, $c \sim 15.05$ Å. In the stacking sequence of the ERI framework, neighbour T6-rings are connected through tilted 4-rings along [001] following the AABAAC… arrangement. This 3-dimensional framework is defined by columns of cancrinite (ε) cages ($[4^6 6^5]$ polyhedra) connected with double 6-ring (D6R) cages (hexagonal prism, $[4^6 6^2]$ polyhedron, formed by two 'A' 6-rings) and columns of erionite cavities ($[4^{12}6^5 8^6]$ polyhedral) between the 'B' or 'C' 6-rings (see Fig. 1; Staples & Gard, 1959; Kawahara & Curien, 1969; McCusker *et al*., 2001; Deer *et al*., 2004; Ballirano & Cametti, 2012). The ε cages are alternatively rotated by 60°. Erionite may occur as a diagenetic product or as a result of hydrothermal alteration in volcanic rock (Passaglia *et al*., 1998). A large chemical variability is typical of this mineral and according to the most abundant extra-framework cation, three different species of erionite have been identified: erionite-Na, erionite-K, and erionite-Ca (Coombs *et al*., 1997; Passaglia *et al*., 1998; Gualtieri *et al*., 1998; Dogan & Dogan, 2008). Previous structural refinements of erionite samples indicate that K^+ cations are located at the centre of the ε cages (Gualtieri *et al*., 1998). Other cations (Na^+, Ca^{+2}, and Mg^{2+}) and water molecules occupy the erionite cages and are distributed on sites located on the symmetry axis (Gualtieri *et al*., 1998). Alberti *et al*. (1997) found that in the erionite cages there are three partially occupied positions Ca1, Ca2, and Ca3 and each is coordinated with water molecules. One additional cationic site

was observed at a special position (½, 0, 0) by Ballirano *et al*. (2009) in erionite-K and labelled as K2. This site corresponds to the K site found by Schlenker *et al*. (1977) in dehydrated erionite-Ca and to the Ca4 site found by Gualtieri *et al*. (1998) in some natural erionite-Ca samples and was attributed to the presence of extra-framework K^{+}, Na^{+}, Ca^{+2} (Ballirano *et al*., 2017).

The growth of the erionite crystals along the *c* axis gives it an elongated morphology that often develops into asbestos-like habit (Belluso *et al*., 2017). As provided by long-term epidemiological studies and several *in vivo* tests, fibrous erionite is responsible for epidemics of malignant mesothelioma (MM) in Cappadocia (Turkey), where three villages (Karain, Tuzköy and Sarihidir) were built with erionite-bearing tuff rocks (Carbone *et al.,*2007; IARC, 2012). MM is a highly aggressive cancer that arises from mesothelial cells of the pleura, peritoneum, and pericardium, with a median survival of about a year from diagnosis (Carbone &Yang 2012). The epidemic of MM in Cappadocia was first described in 1978 by Baris *et al.* (1978) but epidemiological studies of how and why this disease occurs in different groups of people in Cappadocia are still ongoing (Bariş *et al.,*1996; Metintaş *et al.,* 2017). The data acquired to date shows that fibrous erionite is identified as the cause of mesothelioma in over 50% of the population at the three abovementioned villages (Dogan, 2012). In Tuzköy, the annual incidence of MM was estimated at 22 cases per 10000 and it was identical for men and women and the mean age was roughly 50, with a range of 26–75 y (Artvinli &Baris, 1979; Bariş et al., 1978; Simonato *et al*., 1989; Carbone *et al.,* 2007; Emri, 2017). Traces of erionite have been detected in the air and lungs of people of these villages and it has been suggested that inhalation of even small amounts of erionite is sufficient to cause MM (Baris *et al.,*1981; Sebastien *et al.,*1981; Carbone *et al.,* 2007). More recently, erionite exposure issues have also emerged in the USA (Van Gosen *et al.,* 2013). For these reasons, the International Agency for Research on Cancer (IARC) included fibrous erionite in Group 1 "*substance carcinogenic to humans*" (IARC, 2012), and this mineral is considered today similar to or even more carcinogenic than the six regulated asbestos minerals (Wylie, 2017).

Although the toxic and carcinogenic potential of fibrous erionite is out of discussion, the mechanisms by which it induces cyto- and genotoxic damage are not fully understood to date (Gualtieri *et al.,* 2016). Carcinogenesis is a complex phenomenon and multiple factors can contribute to erionite toxicity and MM development: (1) *The morphology of erionite fibres.* As shown in the body of the literature data, length (L) and width (W) of fibres are key factors in the toxicity, inflammation, and pathogenicity of asbestos and erionite fibres (Donaldson *et al.,* 2010; Gualtieri, 2018; Carbone *et al.,* 2019). Fibres with high L/W ratio can reach the low respiratory tract of the lungs and their retention in the parietal pleura leads to the initiation of inflammation and pleural pathology such as MM (Donaldson *et al.,* 2010; Carbone *et al.,* 2019). Fibrous particles with L >8 μm and W <5 μm cannot be eliminated by macrophages (Churg, 1993), leading to an inflammation process known as "frustrated phagocytosis" (Gualtieri, 2018). (2) *Genetics influences*. Recent studies showed that specific genetic mutations of mesothelial cells (*i.e.* germline BAP1 mutations) increase the susceptibility to develop MM at very low levels of erionite exposure (Carbone *et al.,* 2013; Carbone *et al.,* 2019). (3) *The iron-bearing particles*

present at the erionite surface. These impurities may be responsible for carcinogenic activity namely via free radical production (Gualtieri *et al.,* 2016). According to the model described in Gualtieri *et al.* (2016), surface particles may dissolve during phagocytosis when the erionite fibres are engulfed in the phago-lysosome sacks at pH = 4–4.5. Dissolution may leave a residue of iron atoms at specific sites anchored to the surface windows of the 6-membered rings. These surface sites can be responsible to produce H_2O_2 accountable for adverse effects at the cellular and subcellular levels. (4) *The high biopersistence* (*i.e.* the ability to persist in the human body to physico-chemical processes such as dissolution, leaching, breaking, splitting, mechanic clearance) of erionite fibres. Acid zeolites like erionite with Si/Al ratio >2.5 show little to null dissolution in an acidic environment (like the extracellular environment of the lung) because the expected dealumination process does not eventually cause the collapse of the framework (Gualtieri *et al.,* 2018).

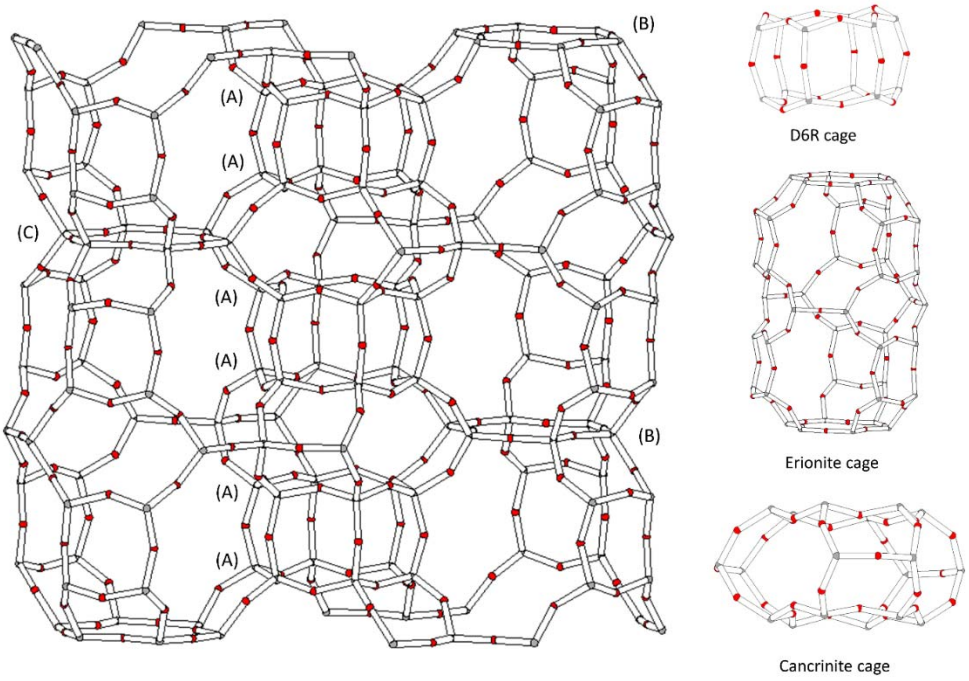

Figure 1. The erionite structure consists of 6-ring (D6R) cages (A), columns of erionite cavities (B) and cancrinite (ε) cages (C).

(5) *The cation exchange capacity of erionite*. In contact with the extracellular and intracellular solutions, erionite fibres may induce ion exchange with the release of extra-framework metals in the lung environment (Gualtieri *et al.,* 2019) and alteration of the cell homeostasis (Di Giuseppe *et al.,* 2022).

In the literature, many authors reported the mineralogical and chemical characterization of a wide range of erionite samples (see for example, Ballirano *et al.,* 2017 and references therein) in the attempt to

correlate the toxicity/pathogenicity mechanisms of fibrous erionite to its mineralogical and microstructural properties. However, until now no one has presented crystal structure data of carcinogenic fibrous erionite from the three villages of the Cappadocia region. The present work aims to fill this gap, and for the first time, it reports the crystal structure of a single erionite fibre from Tuzköy village, determined by synchrotron nano-diffraction. In view of drawing a general model of toxicity/carcinogenicity of Turkish's fibrous erionite and elucidating the trigger mechanisms of MM, a detailed crystal structure investigation of this zeolite is a fundamental step.

2 Experimental

2.1 Geological Overview

The fibrous erionite selected for the study is from Tuzköy, a village located at the junction of the Derinoz and Kizilirmak Rivers in the Nevşehir province (Cappadocia, Turkey). A detailed geological description of this area is reported in Temel & Gündoğdu (1996). Tuzköy village is situated near an erionite-bearing outcrop of the Zelve ignimbrite unit (upper Miocene). This geological unit is characterized by a basal pumice fall layer and was formed by several pyroclastic units that cover an area of about 4200 km^2 in the north of Nevsehir (Temel & Gündoğdu, 1996). Erionite has crystallized with other zeolites (mainly clinoptilolite and chabazite) through hydration reactions (diagenetic processes) from the amorphous aluminosilicate glass of the pyroclastic material deposited in alkaline and saline environments (Temel & Gündoğdu, 1996; Dogan, 2003).

2.2 Thermogravimetric and differential thermal analysis (TG-DTA)

The evolution of the release of volatiles from the samples was analysed by thermo-gravimetric and differential thermal analysis (TG-DTA) using a simultaneous differential thermal analysis (SDTA) SEIKO SSC/5200 SII instrument. Data were collected in the air with a flow rate of 2 μL/min, in the range of 27–1112 °C, and with a heating rate of 10 °C/min.

2.3 Micro-Raman analysis

The sample of erionite from Tuzköy (Turkey) was analysed by μ-Raman spectroscopy. The fibrous powdered sample has been prepared for the analysis in a sealed configuration, working in a fume hood: a small amount of powder (≤ 1mg) has been stuck to a double-sided tape adhering to a microscope glass. The powder has been covered by a coverslip and sealed to the glass substrate. Fibrous erionite from Jersey (Nevada, USA) has been analysed in the same sealed configuration as the reference. An offretite crystal from Saviore dell'Adamello, Brescia (Italy) has been used to discriminate any presence of offretite in the sample.

The μ-Raman measurements have been performed with two spectrometers. The fibrous content has been examined with a HORIBA Jobin Yvon LabRam HR Evolution confocal micro-spectrometer (800 mm focal length), using a He-Ne 632.8 nm laser line as excitation source, with an integrated Olympus BX41 microscope with 5×, 10×, 50× ULWD and 100× objectives, a 600 grooves/mm grating, an XYZ motorized stage and liquid nitrogen cooled silicon CCD. The pinhole has been fixed at 100 μm to reduce the upper glass contribution. The spectral resolution is about 2 cm^{-1}. Minor mineral phases and iron-containing compounds in the sample have been analysed with a HORIBA Jobin Yvon LabRam confocal micro-spectrometer (300 mm focal length), using a He-Ne 632.8 nm laser line as excitation source, with an integrated Olympus BX40 microscope with 4×, 10×, 50× ULWD and 100× objectives, an 1800 grooves/mm grating, an XY motorized stage and a Peltier cooled silicon CCD. The spectral resolution is about 2 cm^{-1}. The systems have been calibrated using the 520.6 cm^{-1} Raman peak of silicon. The spectra have been recorded in the 100-1200 cm^{-1} spectral region with typical exposures of 30 s repeated at least 10 times. Data analysis has been performed by *LabSpec 5* built-in software. Fit with bands deconvolution has been carried out with Gauss-Lorentzian functions.

2.2 X-ray powder diffraction (XRPD)

The fibrous erionite sample studied in this work has been extracted from a friable yellowish tuff in which the fibres crystals were not visible to the naked eye. To obtain the full mineralogical composition, of the whole tuff, it was ground with ethanol, to prevent fibres dispersion, and the resulting powder homogenized into an agate mortar. The mineralogical composition of the sample was determined by X-Ray Powder Diffraction (XRPD). The pattern was collected using a conventional Bragg-Brentano Philips diffractometer (model PW-1729), with θ–2θ geometry, CuKα radiation, 40 kV, 30 mA, and a KSA Energy dispersive detector. The powder was loaded on an aluminium sample holder. Data were collected in continuous mode with a 2 mm fixed divergence and anti-scatter slits mounted in the incident beam. An integrated step-scan of the detector of 0.02 °2θ was used with a time of 25 s, from 3 to 55 °2θ. Phase identification was performed using the search-match procedure developed in *Match! (Crystal Impact)*. Instrument parameters and crystal structure data for each phase present in the samples were fed into the TOPAS5 suite (Coelho, 2018). Background coefficient (polynomial function), lattice parameters, zero-shift error, scale factor, peak shape parameters, and absorption coefficient have been refined.

2.3 Scanning Electron Microscopy (SEM)

Qualitative observations of mineral fibres inside the sample were performed by scanning electron microscopy (SEM). SEM analyses were performed using a FEI Nova NanoSEM 450 FEG-SEM equipped with an X-EDS Bruker QUANTAX-200 system, with 20 kV accelerating voltage, 5 mm working distance and 3.5 μA beam current. A small amount of ungrounded sample was mixed with 1

ml of water. A drop of the suspensions was laid on a carbon tape mounted on an Al stub, left to air dry and gold coated (10 nm of thickness). Images were collected using the signal of both back-scattered and secondary electrons. The surface of the samples was investigated, working at different magnification levels. Length (L) and width (W) of fibres were determined on about 110 individual particles, using 30 SEM images. L and W were calculated using ImageJ image analysis software, version 1.52a (NIMH, 2018). X-EDS (Energy Dispersive X-Ray Spectroscopy) data were collected for the qualitative determination of the chemical composition of erionite fibres.

2.4 Transmission Electron Microscopy (TEM)

Three dimensional-electron diffraction (3DED) data (Kolb *et al*., 2007; Mugnaioli *&* Gemmi, 2018; Gemmi *et al*., 2019) were collected with a Zeiss Libra TEM operating at 120 kV and equipped with a LaB_6 source. 3DED acquisitions were performed in STEM mode after defocusing the beam to have a pseudo-parallel illumination on the sample. A beam size of about 150 nm in diameter was obtained by inserting a 5 μm C2 condenser aperture. An extremely mild illumination was adopted to avoid any alteration or amorphization of the sample.

3DED data were collected in discrete steps of 1° on ten crystals previously identified by energy dispersive X-ray spectroscopy (EDS). Data for structure solution of erionite were taken with a processing beam with an inclination angle of 1° (Vincent *&* Midgley, 1994; Mugnaioli *et al*., 2009), obtained by a Nanomegas Digistar P1000 device. The best-3DED data set on erionite included a total tilt range of 95°. Camera length was 180 mm, with a theoretical resolution limit of 0.75 Å. ED data were recorded by an ASI Timepix detector, able to record the arrival of single electrons and deliver a pattern that is virtually background-free. Data were analysed by ADT3D (Kolb et al., 2011) for cell and space group determination and by PETS2 (Palatinus et al., 2019) for intensity integration. *Ab-initio* structure determination was obtained by direct methods implemented in the software SIR2014 (Burla *et al*., 2015). Data were treated with the kinematical approximation (I_{hkl} proportional to F^2_{hkl}).

2.5 Quantitative chemical analysis (EPMA)

Quantitative chemical composition of the fibrous erionite was obtained at the Department of Earth Sciences, University of Milan, using a JEOL 8200 SuperProbe Electron Probe Microanalyzer equipped with a Wavelength-Dispersive X-Ray (WDS) spectrometer system, W hairpin type filament. The detectable wavelength is 0.087 to 9.3 nm. Atomic number resolution on BSE (Z): less/equal than 0.1 (CuZ). The following analytical conditions were used: excitation voltage of 15 kV, specimen current of 5 nA, peak-count time of 30 s, and background-count time of 10 s. The instrument is also equipped with an EDX system characterized by a detectable element range: Na to U, energy resolution: 144 eV, and lithium (Li)-doped silicon single-crystal semiconductor detector. The following elements were measured at each analytical spot: Si, Al, Mg, Ca, Na, K, Fe, and Ba. Calibration used a set of standards: omphacite for Na, orthoclase for K, forsterite for Mg, fayalite for Fe, and grossular garnet for Al, Si,

and Ca. The raw data were corrected for matrix effects using the Phi-Rho-Z method from the JEOL series of programs.

2.6 Nano single crystal diffraction

Erionite fibres were manually separated from the tuff matrix under a stereoscopic optical microscope. Several crystals were glued onto MiTeGen microloopsTM (Fig. S1) and mounted on magnetic supports compatible with the nanoscope station at ID11 (Wright *et al.,* 2020, Giacobbe *et al*., 2021). Single crystal nano-diffraction data sets of the erionite fibre (~350 x 540 nm, see Fig. S2) were collected at the beamline ID11 (ESRF, The European Synchrotron Radiation Facility, Grenoble, France), using a monochromatic beam produced by a bent Si (111) Laue–Laue double-crystal monochromator (38 keV, wavelength λ = 0.3257 Å, relative bandwidth $\Delta\lambda/\lambda \approx 10^{-3}$). Beam-damage tests due to possible beam heating have been performed before the data collection (Lawrence-Bright *et al*., 2021). The diffraction images were collected having the samples mounted 118.81 mm away from a Dectris Photon Counting Eiger2 4M CdTe detector with an array of 2048 × 2048 pixels of 75 µm × 75 µm. Precise calibration of the detector distance and tilts was obtained using a nanocrystalline CeO_2 standard. The tilt of the modules of the detector was corrected by collecting a grid-like image as described in (Wright *et al*., 2022). Diffraction frames were collected with a continuous scan over 360° (slicing the scan every 0.1°) on the most suitable erionite crystal. Three datasets were measured in different positions of the fibre. NeXus/HDF5 data were then converted into the "Esperanto" format using the script Eiger2crysalis, a portable image converter based on the FabIO library to export Eiger frames (including the ones from LImA) to a set of Esperanto frames which can be imported into CrysalisPro (Rigaku, 2015). The converted images were successively indexed and integrated into CrysAlisPro software.

Absorption effects were corrected using *SCALE3 ABSPACK* of *CrysAlis* (Rigaku, 2015) *via* a multi-scan semi-empirical approach. R_{int} values of 5.4% were obtained (with a data resolution of 0.75 Å)

The crystal structure was solved by direct methods using SIR2019 (Burla *et al*., 2015) and refined using SHELXL-2014 (Sheldrick, 2015). The material for publication was prepared by *WinGX* (Farrugia, 2012) and *publCIF* (Westrip 2010). CheckCIF procedure available at *https://checkcif.iucr.org/* was used to validate the obtained model.

Table 1. Crystallographic data of the single-crystal structure refinements of erionite from Tuzköy. Standard deviations are given in parentheses.

Crystal data	
Chemical formula	$Al_{7.38}Ca_{2.61}K_{2.64}Mg_{0.60}Na_{0.12}O_{100.80}Si_{28.53}$
M_r	2838.33
Crystal system, space group	Hexagonal, $P6_3/mmc$
Temperature (K)	293
a, c (Å)	13.2708 (1), 15.0958 (1)
V (Å^3)	2302.40 (4)
Z	1
Radiation type	Synchrotron, λ = 0.3257 Å
μ (mm^{-1})	0.11
Crystal size (mm)	0.02 × 0.01 × 0.001
Data collection	
Diffractometer	Id11 nanoscope
Absorption correction	*SCALE3 ABSPACK*
No. of measured, independent and observed [$I > 2\sigma(I)$] reflections	45831, 1357, 1322
R_{int}	0.054
$(\sin\theta/\lambda)_{max}$ (Å^{-1})	0.714
Refinement	
$R[F^2 > 2\sigma(F^2)]$, $wR(F^2)$, S	0.038, 0.114, 1.09
No. of reflections	1357
No. of parameters	109
No. of restraints	39
$\Delta\rho_{max}$, $\Delta\rho_{min}$ (e Å^{-3})	1.08, −0.46

Results

3.1 TG-DTA

Thermal analysis of the bulk sample is reported in Fig. S3. The sample exhibits three main endothermic events which occur with maximum reaction rates at about 72.7, 149, 657 and 830 °C. The weight losses corresponding to the first two thermal events are 1.46 % and 3.88 % respectively. These thermal events are related to the release of water that, as typical in many zeolites or zeolites-based materials, begins from early heating stages (Scapino *et al.,* 2017; Arletti *et al.,* 2018). The third main thermal event around 657 °C (weight loss, 8.43 %) is related to dehydroxylation reactions (Ward, 1972). The fourth event at

830 °C corresponds to the release of CO_2 following the decomposition of carbonates (Mertens *et al.,* 2007).

3.2 Raman spectroscopy

The Raman spectra of the erionite from Tuzköy and the erionite reference are shown in Fig. S4. Although natural erionite and offretite can intergrowth, the presence of offretite has been discarded in the sample from Tuzköy, as μ-Raman analysis can reliably assess the presence/absence of the two phases. Raman spectra acquired on the fibres correspond to the zeolite erionite, while the offretite contribution has not been detected (the characteristic peak of offretite at 431 cm^{-1} is absent). The Raman spectrum of an offretite crystal with its distinctive habit from a typical locality where this zeolite has been found (Saviore dell'Adamello, Brescia, Italy) is also reported in Fig. S4 (Passaglia *et al.,*1998; Guastoni *et al.,* 2002).

The main Raman features of erionite are observed in the spectral region between 400 and 600 cm^{-1}, which are assigned to the bending motion of T-O-T bonds in tetrahedra with T=Si, Al. The most intense band has been deconvoluted into two contributions, at 487 and 468 cm^{-1}, respectively (inset in Fig. S4). Other bending signals are found at ~340 and ~570 cm^{-1}. A low-intensity signal is observed at ~1040 cm^{-1}, corresponding to the asymmetric stretching vibration of the Si-O bonds. In the low-wavenumber region, a Raman band at ~130 cm^{-1} is assigned to the lattice modes within the tetrahedra of the zeolites (Knops-Gerrits *et al.,*1997; Wopenka *et al.,*1998). Within the sample, minor mineral phases have been detected, in addition to the erionite contribution, as confirmed by the XRPD analysis. Colourless crystals of quartz and feldspars are mixed with the fibres. The Raman spectra of quartz and albite are shown in Fig. S5, showing the main Raman features. Micrometric crystals with orange to brownish colour have also been found mixed with the fibres, showing the presence of iron-containing compounds (Fig. S6). They consist mainly of hematite, while the presence of goethite and magnetite is rare.

3.3 XRPD

The quantitative phase analysis (QPA) performed using the Rietveld method, shows that the Tuzköy`s tuff contains erionite 42.64(4) wt%, clinoptilolite 24.8(4), quartz 13.0(1) wt%, sanidine 7.59(4) wt%, hornblende 5.28(4) wt%, albite 5.05(2) wt% and mica 1.63(1) wt%. The agreement indices of the Rietveld quantitative phase analysis are: R_{exp}= 3.133, R_{wp}= 11.780%, R_p=8.425%. The graphical output of the Rietveld refinement is shown in Fig. S7.

3.4 SEM

A gallery of collected SEM images is reported in Fig. 2. The Tuzköy`s tuff is mainly composed of fibrous erionite crystals grouped in stocky bundles (Fig. 2a,b,c) with variable width (W: between 2 to 11 μm) and length (L: between 15 to 47 μm). These bundles have a great tendency to slit into very fine fibrils (Fig. 2d). The individual fibrils are dispersed into the matrix (Fig. 2a). The morphology of the erionite fibres is prismatic or acicular and generally longer than 5.0 μm. They have a width ranging from 0.16 to 4.2 μm (Table S1). Summary statistic of erionite fibres geometry (over 110 fibres) is reported in. Table S1. All of the observed fibres have a length/width ratio >3:1. The X-EDS spectra were acquired on the bundles and single fibres (Fig. S8).

Coherently with literature data, X-EDS data revealed the occurrence of Ca, Mg and K as extra-framework ions (Fig. S8c). Also, a small amount of Fe content was detected (Fig. S8d). However, high-resolution FEG-SEM images highlighted the presence of nanoparticles (with variable sizes) located at the bundle's surface (Fig. S8b). It has already been shown that the presence of Fe in the erionite chemical analyses can be attributed to these impurity phases (Gualtieri *et al.,* 2016; Cametti *et al.,* 2013).

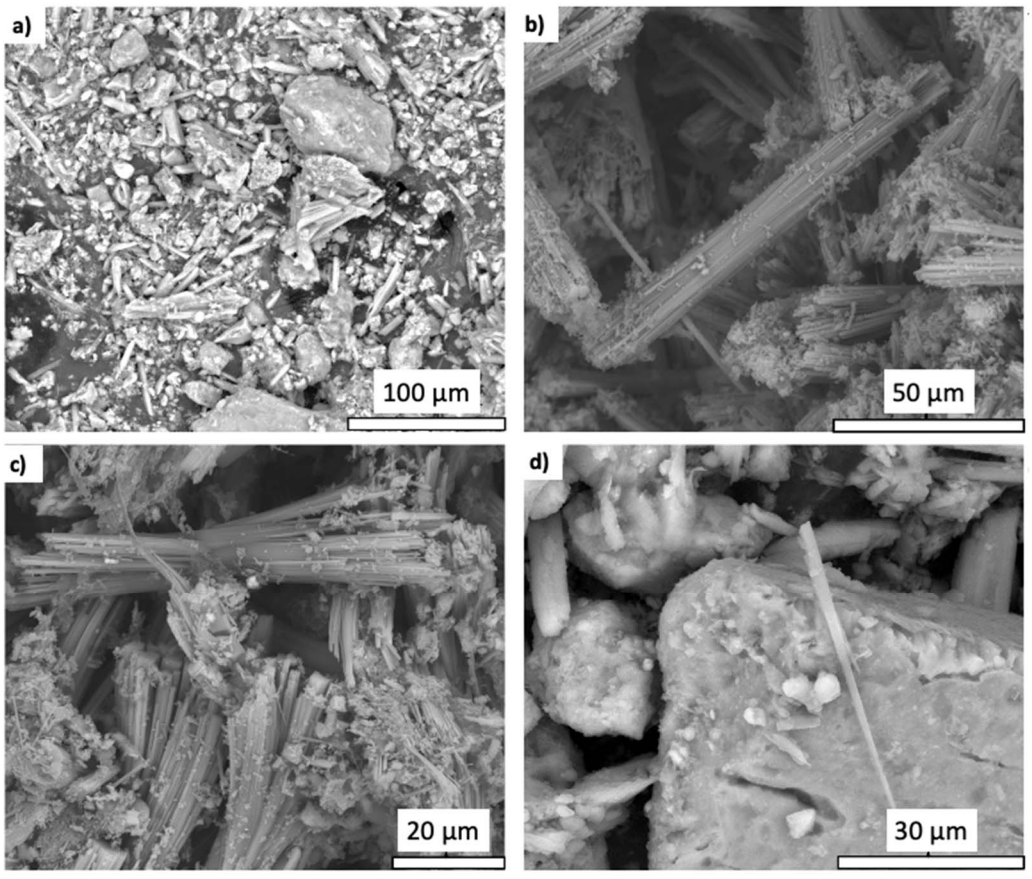

Figure 2. SEM pictures of Tuzkoy's tuff and erionite fibres. a) General overview of the sample (tuff). Erionite fibres are scarce in the matrix. b,c) Representative high-resolution SEM-FEG images of fibres bundles. Erionite fibrils are grouped in tabular bundles with variable width (W: between 2 to 11 μm)

and an average length of 31 μm (L: between 15 to 47 μm). d) Single fibril of erionite found in the sample.

3.5 TEM

TEM investigation was primarily performed to assess whether erionite from Tuzkoy presents offretite disordered sequences. Fig. 3 shows typical bundles of erionite fibrils. TEM images confirmed that the variability of bundle dimensions is in line with the SEM study. As already described by Matassa *et al.* (2015), erionite tips often display a fringed appearance (Fig. 3b and 3c). This evidence confirms that what is considered a fibre is actually a bundle of fibrils with a thickness of only a few tens of nanometers.

Several energy Dispersive X-ray (EDX) spectra coupled with 3DED (3D-electron diffraction) were collected along thin erionite bundles or at the very tip of larger bundles.

Representative chemical analyses are reported in the Fig. 3b and Fig.3c. The red circles indicate the areas from which the chemical analyses were performed. The ribbon-like bundles revealed, in agreement with Ballirano *et al.* (2015), the occurrence of Mg, Ca, K, Al and Si and, for some of them a not negligible amount of Fe. As demonstrated in Gualtieri *et al*. (2018), Fe is not part of the erionite crystal structure but is associated with impurities mostly concentrated at the surface of the fibres. Cross-fibres EDS profiles show no significant change in chemical composition, ruling out the occurrence of clear polytypic sequences connected with chemical variations.

Although a relatively high Mg content was found, 3DED confirmed that all the specimens were characterised by cell parameters consistent with erionite, and not with offretite. Although 3DED data did not prove to be as 'sensitive' as synchrotron nano-diffraction for the extra-framework content, they allowed us to solve *ab-initio* the typical zeolite framework of erionite and to locate the K ion in the cancrinite cage, enforcing the evidence that offretite was not present.

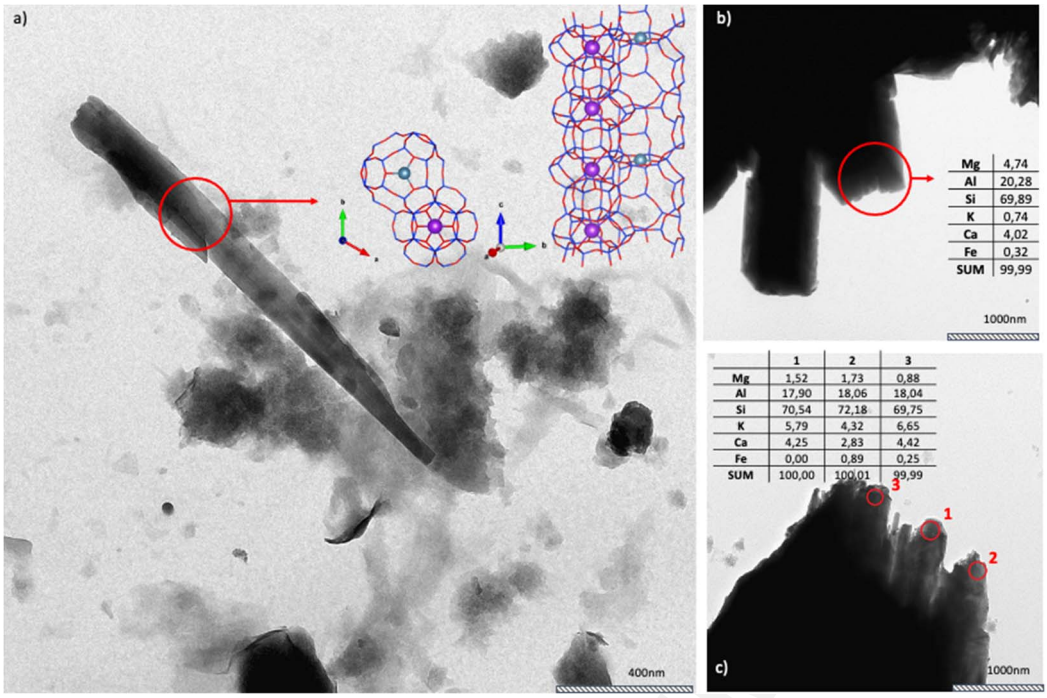

Figure 3 TEM image of erionite fibre bundles. a) A relatively thin erionite fibre with thickness of about 150 nm, from which a rather complete 3DED data set was collected. *Ab-initio* structure solution performed based on this dataset allowed us to identify the erionite framework, which is overlapped in the figure. b-c) Typical fringed appearance of large erionite bundles. Chemical analysis (several energy Dispersive X-rays) performed on the red spots confirm a chemistry in line with the erionite (data in %).

3.6 EPMA

The results of the EPMA analyses expressed in weight percent with standard deviations are reported in the Supplementary materials (Table S2). Erionite chemical formula was calculated after renormalization of the chemical analyses hypothesizing a water content of 18.5 wt% (corresponding to ~30 water molecules per formula unit). The resulting chemical formula $(K_{2.63}Ca_{1.57}Mg_{0.76}Na_{0.13}Ba_{0.01})[Si_{28.62}Al_{7.35}]O_{72}\cdot 28.30H_2O$ was obtained from the average of the chemical analyses of each sample passing the balance error (E%) (Passaglia, 1970).

3.7 Single Crystal Diffraction

The structural parameters of the erionite from Tuzköy collected at ID11 (ESRF) are reported in Table 1 and Fig. 4a and b. It crystallizes in the hexagonal system, and systematic absences were consistent with the space group $P6_3/mmc$. The unit cell parameters $a=b$=13.2708 (1) Å, c=15.0958 (1) Å and volume V= 2302.40 (4) Å^3 are slightly smaller than the ones in the models previously proposed by

Alberti *et al*. (1997), Gualtieri *et al.* (1998), Ballirano *et al.* (2009), and Cametti *et al.* (2013), showing that the 'individual' information derived from single crystal diffraction data is close to the literature bulk information based on powder data (*i.e.*, the *c*/*a* ratios of the model described below are identical within 1σ).

The refinement converged at $R[F^2 > 2\sigma(F^2)]= 0.038$, $wR(F^2)= 0.114$, $S=1.09$. The analysed fibre is a fibril with a section whose diameter is about 200-300 nm isolated from larger 'bundles' of fibres.

The chemical partition after the final refinement is: $(K_{2.64}Ca_{2.61}Mg_{0.60}Na_{0.12})[Si_{28.53}\ Al_{7.38}]O_{100.80}$ (omitting the contribution of the H atoms), in line with the calculated chemical analysis $(K_{2.63}Ca_{1.57}Mg_{0.76}Na_{0.13}Ba_{0.01})[Si_{28.62}Al_{7.35}]O_{72}\cdot 28.30H_2O$, exception made for undetected traces of Ba and higher content of Ca. Fractional coordinates, site partition (s.p.) atomic displacement parameters, and site symmetry (s.s.) are reported in Table 2, and relevant bond distances are supplied in Table 3.

Framework

Two crystallographic independent tetrahedral sited were refined: T1 and T2 sites, respectively occupied by Al1 and Si1 (for T1) and Al2 and Si2 (for T2). These two sites, sitting on the positions x/*a*= 0.23398(4), y/*b* = 0.99977(3) and z/*c*= 0.10458(3) and x/*a*= 0.33174(4), y/*b* = 0.90620(5) and z/*c*= 0.2500, build respectively the D6R and S6R cages. Al1 and Si1, as well as Al2 and Si2, share the same site and as such, their anisotropic thermal factors and occupancies have been constrained during the refinement. The partition between Al and Si over the two crystallographic sites has been fixed such as Si is the dominant chemical species (79.57%) while Al corresponds to the remaining 20.43% of the total population of the two sites to follow the chemical analysis.

The mean bond distances <T1-O> = 1.637 Å and <T2-O>= 1.633 Å indicate a very small difference between the mean [T-O] distances of the two tetrahedral sites (<T1-O> - <T2-O> is only 0.004 Å). Application of the Jones' determinative curves (Jones, 1968) indicates a very small preference of Al for T2 (s.p. = 0.22) with respect to T1 (0.198) in excellent agreement with both chemical data and refined s.p..

Individual T-O-T angles show no deviation from the ones described in Alberti *et al.* (1997) Gualtieri *et al.* (1998) and Ballirano *et al.* (2009).

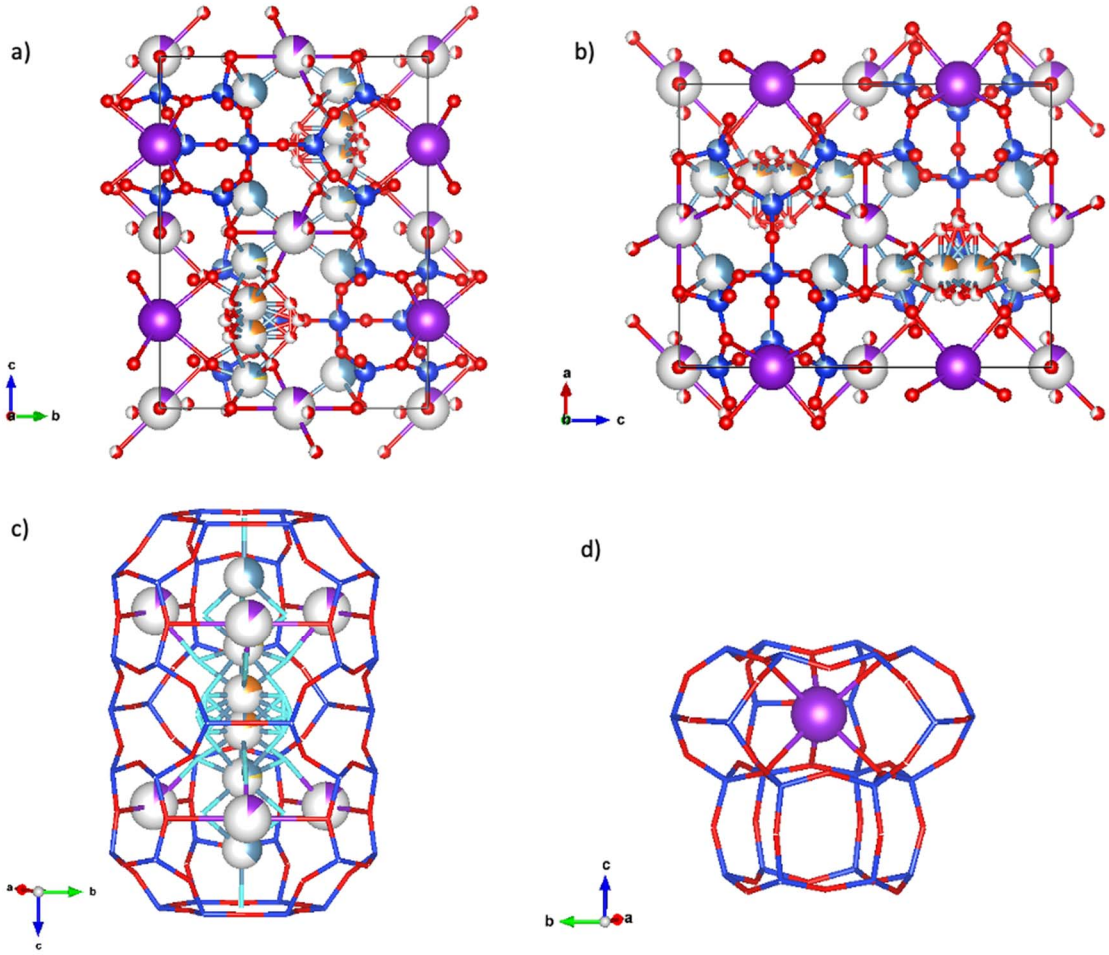

Figure 4 Crystal structure of erionite from Tuzköy (Turkey). a) View of the crystal packing along the *a* axis. b) View of the crystal packing along the *b* axis. c) Detail of the erionite cavity and its extra-framework content. d) detail of the cancrinite cage hosting the K atom. Legend: electric blue balls=Si, red balls = O atoms (also H_2O molecules), ice blue balls= Ca, yellow balls= Na, orange balls=Mg, purple =K. The plots were created using the *VESTA* software (Momma & Izumi, 2011).

Extra-framework

The positions of the extra-framework atoms were identified by a careful inspection of the electron-density map calculated by Fourier difference synthesis and the species were assigned based on the chemical characterization by choosing the association that minimized the *RF* of the refinement to 3.8%. The extra-framework content is found as in the following.

The cancrinite cage hosts K atom (*i.e.*, K1) as shown in Fig. 4d. This site is fully occupied, in line with the chemical characterization. As reported in the work of Gualtieri *et al.* (1998), this site may be fully occupied, as in the case of Lady Hill and Shourdo erionites, or only partially (down to 85%) as in the case of the erionites found in Tunguska. K1 atom is 12-fold coordinated with 6 O2 atoms (2.923 Å) and 6 O3 atoms (3.376 Å). K1-O3 distance is longer than the K1-O2 distance. This difference is well

reported in Cametti *et al.* (2013) for the woolly Erionite-Na from Oregon. Another K site, K2, in position x/*a*= 0.5, y/*b* = 1 and z/*c*= 0, has been found with a site occupancy of 10%. K2 is coordinated to two O4 atoms (3.119 Å), four O1 atoms (3.276 Å), two WA3C (2.65 Å) and two WA1B (3.3192 Å). Several cation positions have been found in the erionite cage at different z/*c* heights as visible in Fig. 4c.

The refinement has indicated that the extra-framework cations are located at three Ca1, Ca2, and Ca3 sites, with the Ca2 and Ca3 sites partially substituted by Na and by all available Mg, respectively. As well, we have identified six water molecules sites.

The refined Ca population in the erionite from Tuzköy presents a higher value than that reported in the chemical analysis. As in Alberti *et al.* (1996) this difference can be explained by cation migration during the analysis or by the intrinsic difference of a bulk vs a single fibre/crystal analytical technique.

Ca1 site is partially occupied and sits, along the axis of the erionite cage, at z/*c*= 0.4016(14). The z/*c* coordinate is slightly displaced from the threefold axis. Ca2 site is shared with Na2 atom. Due to some instabilities during the refinement, Na2 occupancy has been constrained in such a way respecting the same partition as derived from the chemical analysis, while the occupancy of the Ca2 has been set free to be refined. Both Ca2 and Na2 have been constrained to the same anisotropic thermal factors.

The last site is Ca3, which is shared with Mg3 atom. As already observed by other authors (Ballirano *et al*., 2009), some difficulties have been encountered when modelling the occupancies of this site. This site results partially occupied at 21 % (value originally obtained by refining the occupancy in the hypothesis that only Ca3 was present). The total content in Mg is in line with other erionites (see the woolly sample from Durkee, Oregon in Cametti et al., 2013).. Higher values can be used in the discrimination between erionite and offretite. To rule out the presence of the latter, we have performed a further crystallographic test, that will be discussed in the following section.

According to the bond analysis (below 3.3 Å) (Table 3) and Fig. 5, Ca1, is surrounded by three H_2O molecules WA1B at distance of 2.33 Å, three WA5B at distance of 3.13 Å and one WA1 at a distance of 2.29 Å. Ca2 (site shared with Na2) is connected instead to nine H_2O molecules (three WA3C at 2.06 Å, three WA1B at 2.26 Å and three WA2B at 2.54 Å, respectively). Ca3 (site shared with Mg) is coordinated to nine water molecules, *i.e*., six WA2B (three of them at distance of 1.77 Å and the rest at distance of 2.25 Å) and three WA3C at distances of 2.20 Å. Six is the total number of H_2O sites found by difference Fourier map; these are all located in the erionite cage as shown in Fig. S9. Concerning the water molecule positions, some differences are found with respect to the model described in Cametti *et al.* (2013), Ballirano *et al.* (2009) and Gualtieri *et al.* (1998) but this is not surprising because the content and position of H_2O molecules in erionite samples is extremely variable. All water site occupancies have been refined and are displayed in Fig. S9. ISOR weak restraint for all the oxygen atoms of the water molecules has been applied to allow approximately isotropic refinement.

PLAT260_ALERT_2_B concerning respectively atom WA1B and WA5B may be attributed to solvent disorder in the erionite channels.

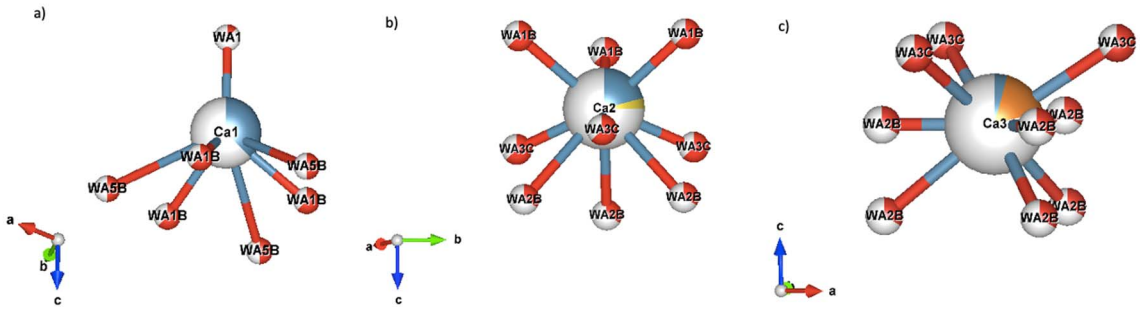

Figure 5 Ca site coordination (below 3Å) along the [110] direction. a) Ca1 coordinated to 3 ×WA1B, 3x WA5B and one WA1. b) Ca2 (partially occupied by Na2) coordinated to 9 H_2O (3 × WA3C, 3 × WA1B, and 3 × WA2B).c) Ca3 is coordinated to 6 × WA2B and 3 × WA3C. Legend: red balls = O atoms representing H2O molecules, ice blue balls = Ca, yellow balls = Na, orange balls =Mg. The plots were created using the VESTA software (Momma & Izumi, 2011)

Table 2. Site symmetry (s.s.), site partition, final atomic coordinates, and atomic displacement parameters (Å^2) for the erionite from Tuzköy.

site	s.s.	site partition	x/a	y/b	z/c	U_{eq}	U^{11}	U^{22}	U^{33}	U^{23}	U^{13}	U^{12}
Si1	1	0.804(15)	0.23398(4)	0.99977(3)	0.10458(3)	0.01710(18)	0.0223(3)	0.0172(2)	0.0127(2)	0.00090(11)	-0.00166(13)	0.01053(16)
Al1	1	0.198(15)	0.23398(4)	0.99977(3)	0.10458(3)	0.01710(18)	0.0223(3)	0.0172(2)	0.0127(2)	0.00090(11)	-0.00166(13)	0.01053(16)
Si2	m..	0.77(3)	0.33174(4)	0.90620(5)	0.25	0.0152(2)	0.0138(3)	0.0175(3)	0.0160(3)	0	0	0.0092(2)
Al2	m..	0.22(3)	0.33174(4)	0.90620(5)	0.25	0.0152(2)	0.0138(3)	0.0175(3)	0.0160(3)	0	0	0.0092(2)
K1	-6m2	1	0	1	0.25	0.0341(3)	0.0355(5)	0.0355(5)	0.0313(7)	0	0	0.0178(2)
K2	.2/m.	0.105	0.5	1	0	0.152(15)	0.082(11)	0.23(4)	0.19(3)	-0.06(3)	-0.032(14)	0.12(2)
Ca1	3m.	0.39(3)	0.333333	0.666667	0.4016(14)	0.29(2)	0.31(2)	0.31(2)	0.26(2)	0	0	0.155(12)
Ca2	3m.	0.206(12)	0.666667	1.333333	0.4185(14)	0.132(9)	0.084(7)	0.084(7)	0.23(2)	0	0	0.042(3)
Na2	3m.	0.033	0.666667	1.333333	0.4185(14)	0.132(3)	0.084(2)	0.084(2)	0.228(7)	0	0	0.0421(10)
Ca3	3m.	0.06(2)	0.666667	1.333333	0.2951(12)	0.084(6)	0.038(4)	0.038(4)	0.176(17)	0	0	0.0190(19)
Mg3	3m.	0.15(3)	0.666667	1.333333	0.2951(12)	0.084(6)	0.038(4)	0.038(4)	0.176(17)	0	0	0.0190(19)
O1	1	1	0.32241(13)	0.97215(14)	0.16105(9)	0.0365(3)	0.0393(7)	0.0485(8)	0.0303(6)	0.0108(6)	-0.0008(6)	0.0285(6)
O2	.m.	1	0.09775(9)	0.90225(9)	0.12618(13)	0.0318(4)	0.0262(5)	0.0262(5)	0.0352(9)	-0.0019(4)	0.0019(4)	0.0071(7)
O3	.m.	1	0.25212(19)	1.12606(9)	0.13524(11)	0.0336(4)	0.0523(11)	0.0293(6)	0.0270(8)	-0.0035(4)	-0.0070(8)	0.0261(6)
O4	.2.	1	0.26497(18)	1	0	0.0325(4)	0.0421(8)	0.0375(10)	0.0164(7)	-0.0004(6)	-0.0002(3)	0.0187(5)
O5	mm2	1	0.23098(12)	0.76902(12)	0.25	0.0361(6)	0.0241(8)	0.0241(8)	0.0548(17)	0	0	0.0082(10)
O6	mm2	1	0.45857(13)	0.9171(3)	0.25	0.0346(6)	0.0233(8)	0.0440(15)	0.0434(14)	0	0	0.0220(8)
WA1B	1	0.62(4)	0.506(2)	1.2529(10)	0.5049(17)	0.36(2)	0.17(2)	0.47(4)	0.34(3)	0.024(8)	0.048(16)	0.087(11)
WA2B	.m.	0.35(6)	0.513(3)	1.2565(13)	0.203(4)	0.123(15)	0.066(11)	0.138(13)	0.14(3)	-0.014(7)	-0.027(15)	0.033(6)
WA3C	.m.	0.61(4)	0.837(2)	1.4185(11)	0.3758(15)	0.244(16)	0.29(3)	0.223(16)	0.24(3)	0.049(9)	0.098(19)	0.147(15)
WA4C	m..	0.30(10)	0.485(5)	1.242(3)	0.25	0.116(14)	0.10(2)	0.16(2)	0.06(3)	0	0	0.049(11)
WA1	-6m2	0.12(4)	0.333333	0.666667	0.25	0.14(6)	0.09(5)	0.09(5)	0.24(11)	0	0	0.05(3)
WA5B	1	0.50(4)	0.4486(18)	0.897(4)	-0.012(4)	0.39(4)	0.176(18)	0.47(6)	0.63(8)	-0.09(5)	-0.04(2)	0.23(3)

Table 3. Relevant bond distances (Å) of erionite from Tuzköy (Turkey) (T1= Si1, Al1, T2= Si2, Al2).

T1-O4	1.6311(7)	Ca1-WA1B x 3	2.33(3)
T1-O1	1.6334(13)	Ca1-WA1	2.29(2)
T1-O3	1.6363(7)	Ca1-WA5B x 3	3.13(5)
T1-O2	1.6462(8)	Ca1-Ca2	2.72(3)
mean	1.63675	Ca2-Ca3	1.86(2)
Delta (Δ)	0.0012247		
T2-O6	1.6154(6)	Ca2-WA3C x 3	2.06(2)
T2-O5	1.6334(9)	Ca2-WA1B x3	2.26(3)
T2-O1 x 2	1.6410(13)	Ca2-WA2B x 3	2.54(7)
mean	1.6327		
Delta (Δ)	0.0040452	Ca3-WA2B x 3	1.77(3)
		Ca3-WA4C x 3	2.20(6)
K1-O2 x 6	2.9228(19)	Ca3-WA2B x 3	2.25(3)
K1-O3 x 6	3.376(2)		
K2-WA1B x 2	3.3192(9)		
K2-WA5B x 2	1.19 (4)		
K2-WA3C x 2	2.65 (3)		
K2-O4 x 2	3.119(2)		
K2-O1 x4	3.2757(14)		

4 Discussion

This study reports the full crystal-chemical and structural characterization of a mesotheliomagenic erionite fibre from Tuzköy (Turkey). We have used the term "killer" fibre because it is universally shared that fibrous erionite is directly responsible for fatal lung malignancies (namely MM) in the population living in the Cappadocian area of Turkey (Carbone *et al*., 2011). The potency of fibrous erionite in inducing mesothelioma in rats has been early observed by Wagner *et al.* (1985). Carthew *et al.* (1992) reported that erionite has 300-800 times more mesothelioma potency than chrysotile and 100-500 times more such potency than crocidolite when given through intrapleural routes in animals. These data are confirmed by other animal studies showing that erionite is 200 times more tumorigenic than crocidolite (Hill *et al.,*1990) and 500–800 times more tumorigenic than chrysotile (Coffin *et al.,*1992). In the Cappadocian region,

exposure to fibrous erionite caused MM epidemic unprecedented in history in the villages of Karain, Sarihidir, and Tuzköy as a result of the inhabitants building their homes from erionite-rich pyroclastic rocks (Carbone *et al.,* 2011).

Although genetic susceptibility has been invoked to explain the aetiology of MM (see below) and especially the high potency of erionite in inducing MM in humans (Carbone & Yang, 2012), the peculiar crystal-chemical-physical properties (surface iron, cation exchange, biodurability) of fibrous erionite and their interplay with extrinsic factors explain its carcinogenic potential. For this reason, the achievement of the crystal-chemistry of the erionite fibre from Tuzköy (Turkey) is like reconstructing the profile of the "killer".

The offretite dilemma

Erionite is often associated to the "sister" zeolite offretite [OFF] with ideal formula $K_2Ca_2Mg_2[Al_{10}Si_{26}O_{72}]\cdot 32H_2O$, hexagonal with unit cell parameters approximately a = 13.29 and c = 7.58 Å, and space group $P\bar{6}m2$ (Passaglia *et al.,*1998). Because erionite-offretite epitaxial growths and disordered erionite-offretite stacking sequences are common (Passaglia *et al.,*1998), especially in Mg-rich samples, there is need for precise identification of the erionite fibre from Tuzköy to rule out that we deal with offretite or an erionite-offretite sequence. This point is very important due to the implication of erionite in causing mesothelioma. If it is discovered that the studied compound is offretite or a mix erionite-offretite instead, there would be resounding implications at health, regulatory and legal levels. First of all, offretite should be explicitly included in the list of IARC carcinogens together with erionite while, at the moment, it is only suspected to have toxic potential similar to that of erionite (Mattioli *et al.,* 2018).

Although it is very tricky to distinguish erionite from offretite because they have similar cation content and crystal structures, the results of our study unequivocally ruled out the possibility that erionite from Tuzköy is actually offretite.

Our attention has first focussed on the Mg content. The Mg values ($Mg_{0.60}$ from the structure refinement and $Mg_{0.76}$ from the EPMA, respectively) indicate that we are in the field of existence of erionite and not in that of offretite. The latter shows a limited variation and Ca/Mg ratio always very close to 1.0 (Passaglia *et al.*, 1998).

On a crystallographic standpoint, the metric relationship existing between the cell parameters of the two structures suggests that most of the Bragg peaks of the two zeolites coincides exactly in their diffraction patterns (Kerr *et al.,*1970; Bennett & Grose, 1978). More in detail, the l=2m ($m\neq 0$) hkl reflections of the erionite are in perfect overlap with the (hkm) reflections of the offretite, as well as the (hk0) of erionite with the (hk0) of the offretite. There are, however, a few relatively strong diffraction lines due to the unit-cell doubling [namely the (101), (201), (211), (213), (311) reflections (Passaglia *et al.,*1998)] that belong only to erionite. The appearance of these reflections is considered as a valid test for the presence of erionite. Fig.

6 shows the assessment of the above mentioned (*hkl*) reflections in the raw images collected during the single crystal experiment.

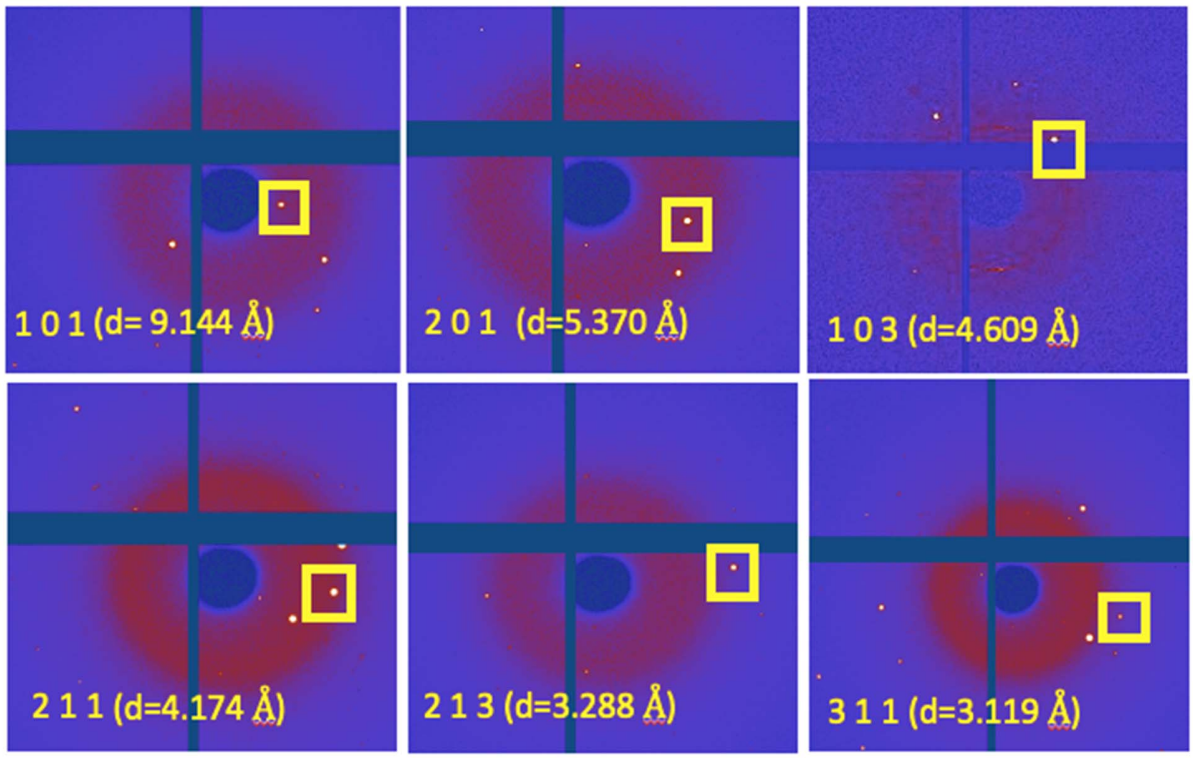

Figure 6. Assessing the presence of the erionite characteristic reflections (101), (201), (211), (213), (311) in the raw images. The cross in the image correspond to a module gap present in the detector Eiger2 4M CdTe. The additional reflection (103), to be ascribed only to erionite, is shown.

Nevertheless, if we consider low-theta (high *d*-spacings) indexes, there is another reflection, namely (103), that the work of (Passaglia *et al.,*1998) does not include in the list. A plausible reason why (Passaglia *et al*., 1998) did not mention these Miller indices may be linked to the fact that this work refers to results obtained from powder diffraction and, in such condition, this reflection results to be in overlap with the (202) one. Considering an additional characteristic reflection could improve the "diagnostic" for testing the effective presence of the erionite.

The test described above, however, does not rule out the presence of offretite, thus a method considering the intensity ratio of Bragg peaks containing only the erionite scattering contribution to those containing both the erionite and the offretite contributions can be used to determine the offretite content in erionite. This method described in (Passaglia *et al.,*1998) has been applied by normalizing the intensity of the 210

peak (present in both erionite and offretite), to clearly show the change in the 210/211 [only observable in erionite, thanks to (211)]. The same method has been applied to our single crystal study (Fig. 7). In our case, the data used for this test were collected at different heights of the investigated fibre which is prismatic and does not have a constant volume exposed to the X-rays. This means that, for different measures in height, the scattering intensity must not be the same. If some intercalation of offretite was present, the ratio between 210 and 211 integrated intensities then would change. For this test, this value remains substantially constant, discarding the possibility of offretite stackings.

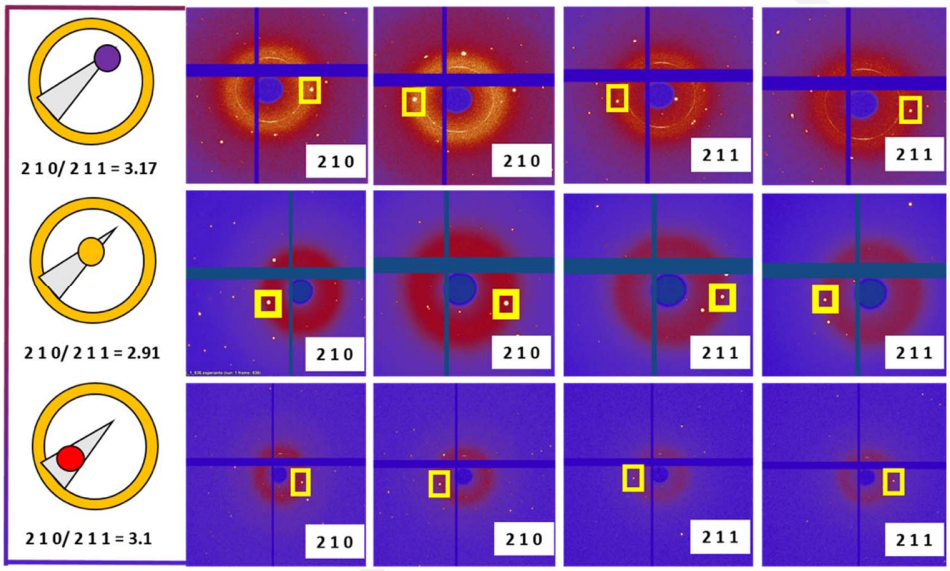

Figure 7 Evaluation of the ratio for the diffraction spots intensities 210/211 to rule out the presence of offretite as described in (Passaglia *et al.*, 1998).

Classification of the erionite fibre

Given that the Tuzköy fibre is not offretite, this species should be classified within the erionite family. The chemical formula calculated from the refinement using single crystal diffraction is $(K_{2.64}Ca_{2.61}Mg_{0.60}Na_{0.12})[Si_{28.53}\ Al_{7.38}]O_{72}\cdot 28.80H_2O$ and indicates an erionite-K/erionite-Ca term. On the other hand, the mean chemical formula obtained from the EPMA is $(K_{2.63}Ca_{1.57}Mg_{0.76}Na_{0.13}Ba_{0.01})[Si_{28.62}Al_{7.35}]O_{72}\cdot 28.30H_2O$ and points to an erionite-K term. The two formulas differ for the Ca content and this can be due to several reasons: i) EPMA data were obtained by averaging various points sampled on several eventually different fibres; ii) chemical characterization was performed using a bulk technique, whereas the crystallographic characterization was performed on a single fibre; iii) erionite possesses intrinsic variability, as also demonstrated by the Energy Dispersive X-ray

(EDX) spectra collected on different erionite fringes; iv) it is known for a long time that the chemical point analysis using sources of electrons can be very difficult (Clark *et al.,*1995) and somehow unreliable when the target is a thin mineral fibre or fibre bundle. This is because there is a strong influence of the shape and thickness of these anisotropic particles on the detected signal (Valdrè *et al.,* 2018); in EDS-based determinations, especially for long times of analysis, possible beam damage of the zeolite fibre and loss of low Z elements, particularly Na, is expected (Dogan, 2012).

The chemical variability of the Cappadocian erionites is confirmed by point chemical analyses determined by Dogan (2012) indicating both erionite-K and erionite-Ca terms with a prevalence of the erionite-K for the TEM-EDS results independently verified by EPMA. Dogan (2012) proposes a mean formula of $(K_{3.09}Ca_{1.57}Mg_{0.55}Na_{0.26})[Si_{28.70}Al_{6.61}Fe_{0.60}]O_{72}$ in agreement with our EPMA-determined formula.

Environmental and health implications of the study

The crystal structure of the mesotheliomagenic erionite fibre from Tuzköy will be of aid for the understanding of the biochemical mechanisms that cause adverse effects *in vivo* and lead to the onset of MM. The profile of this erionite "killer" fibre rules out the role of the other "suspects" offretite or erionite-offretite disordered sequence.

We have seen that Tuzköy fibres are longer than 5.0 μm and display widths in the range of 0.16 to 4.2 μm (Table S1). Geometrically, these erionite fibres cannot negotiate the aperture (3-10 μm wide) of the pleural diaphragmatic stomata and can undergo phagocytosis attempts by phagocytic cells leading to inflammation in the pleural space. Because erionite fibres are biodurable and phagocytosis is inefficient, the inflammation activity is chronic and causes the damage of the DNA of the adjacent mesothelial cells initiating the sequence of adverse effects leading to the onset of MM.

We have seen that the Tuzköy erionite fibre does not host iron in the structure, but micrometric iron-rich particles of hematite and subordinate goethite and magnetite can be found at the surface of the fibres. These iron-rich impurities may be responsible to produce ROS (Gualtieri *et al.,* 2016; Gualtieri, 2018) and they can dissolve during partial phagocytosis when the erionite fibres are engulfed in the acidic phago-lysosome sacks leaving a residue of iron atoms at specific catalytic sites anchored to the surface windows of the 6-membered rings of erionite. The newly formed iron species form cyto/geno-toxic free radicals when they get in contact with H_2O_2 released during phagocytosis.

We have also seen that the Tuzköy fibre is rich in Ca^{++} and K^+ extra-framework cations. These cations can be exchanged in both extracellular and intracellular media and can alter cell homeostasis leading to detrimental cell necrosis (Di Giuseppe *et al.,* 2022). In lung lining fluid of the extracellular environment, the content of cations is: K^+ 6-29 mM, Na^+ 82-132 mM, Ca^{++} 4 mM while in the cytosol (intracellular environment) the content of cations is: K^+ 139-150 mM, Na^+ 12 mM, Ca^{++} 2×10^{-4} mM (Lodish *et al.,*1999;

Innes *et al.,*2021). Considering the cation exchange properties of erionite (with a selectivity series of $Rb^{+} > Cs^{+} > K^{+} > Ba^{++} > Sr^{++} > Ca^{++} > Na^{+} > Li^{+}$: Sherry 1979), the Tuzköy fibre can adsorb and trap K^{+} in its micropores and release Ca^{++} in both extracellular and intracellular environment. The minor amount of extracellular and intracellular Ca^{++} ions can also be exchanged by extra-framework Na^{+} (and eventually Mg^{++}). The Ca^{++} exchange has a paramount role because calcium cross-talk in the cytosol is assumed to be one of the most important biochemical mechanisms controlling cell survival/proliferation. In fact, according to the model delivered by Carbone & Yang (2012), cells with extensive DNA damage caused by exposure to erionite undergo programmed death (apoptosis) and do not grow into malignancies thanks to the action of genes like *BAP1*. In the endoplasmic reticulum (ER), BAP1 protein binds, deubiquitylates, and stabilizes type 3 inositol-1,4,5-trisphosphate receptor (IP3R3), modulating Ca^{++} release from ER into the cytosol and mitochondria to promote apoptosis (Bononi *et al.,* 2017). Reduced levels of BAP1 in the genetically predisposed carriers of the mutated $BAP1^{+/-}$ forms are responsible for the reduction both of IP3R3 levels and Ca^{++} flux, preventing $BAP1^{+/-}$ cells that accumulate DNA damage from executing apoptosis. A higher fraction of cells exposed to erionite survive genotoxic stress, resulting in a higher rate of cell transformation and proliferation and a higher probability of onset carcinogenesis. Ca^{++} exchange induced by erionite can modify cytosol ion concentration and eventually alter the ER-mitochondria cross-talk (calcium ATPase pump) to restrain or interrupt the mitochondrial apoptotic pathways in the same way as the lack of BAP1 (substituted by the modified forms $BAP1^{+/-}$) does. Hence, intracellular Ca^{++} exchange may be a co-factor in determining the mesothelioma-genicity of erionite-like genetic susceptibility.

Finally, it is interesting to remark that the behaviour of erionite-K/erionite-Ca from Tuzköy should be different from that of other erionite species like erionite-Na from Jersey (Nevada, USA) (Gualtieri *et al.,* 2016) for which extracellular/intracellular K^{+} and Ca^{++} exchange by Na^{+} should be more efficient.

More work is needed to understand the cation exchange mechanisms of erionite *in vitro* and *in vivo* as pointed out by Pacella *et al.* (2021) who suggested that the biological effects hypothesized for the released cations (such as Mg^{++} and Ca^{++}) may be investigated by comparing the *in vitro* toxicity of both pristine and modified samples after immersion in lung fluids.

5 Conclusions

This study depicts, for the first time, the full crystal-chemical characterization of an erionite fibre from Tuzkoy (Cappadocia, Turkey). The state-of-the-art combined approach of nano-single crystal X-ray diffraction (nSC-XRD), transmission electron microscopy (TEM), and μ-Raman techniques allowed us to assess that the erionite from Tuzkoy is not associated with offretite. These findings are relevant owing to the implication of erionite causing mesothelioma and at regulatory levels and represent the onset for *in-vivo*

and *in-vitro* studies to understand its toxicity. The exact determination of the extra-framework content, and more precisely K and Ca, is crucial to determine the mechanism by which it may be exchanged in extracellular and intracellular media.

Up to now, most of the erionite crystal structures described in the literature were obtained from powder diffraction methods. These nanometric fibres are difficult to isolate and even more challenging to collect reliable data sets. Thanks to the new upgraded machine of the ESRF- EBS (Extra Brilliant Source) and last generation hybrid photon counting detectors (Eiger2 4M CdTe) it is now possible to collect reliable and complete data sets of nano-sized crystals that allow a very fine study of complicated systems such as this fibrous zeolite.

5 Acknowledgments

The work is supported by the PRIN project fund "Fibres: a multidisciplinary mineralogical, crystal-chemical and biological project to amend the paradigm of toxicity and carcinogenicity of mineral fibres" (PRIN: Progetti di Ricerca di Rilevante Interesse Nazionale—Bando 2017—Prot. 20173X8WA4). The ESRF is acknowledged for the provision of beam time at the beamline ID11. Authors thanks Mauro Gemmi for the technical TEM support at IIT@NEST, Pisa.

References

Alberti, A., Cruciani, G., Galli, E. & Vezzalini, G. (1996). *Zeolites*, **17(5-6)**, 457-461.

Alberti, A., Martucci, A., Galli, E. & Vezzalini, G. (1997). *Zeolites*, **19**, 349-352.

Arletti, R., Fantini, R., Giacobbe, C., Gieré, R., Vezzalini, G., Vigliaturo, R. & Quartieri, S. (2018). *Am. Mineral.* **103**, 1741-1748.

Artvinli, M. & Bariş, Y. İ. (1979). *J. Natl. Cancer Inst.* **63(1)**, 17-22.

Ballirano, P., Andreozzi, G. B., Dogan, M. & Dogan, A. U. (2009). *Am. Mineral.* **94**, 1262-1270.

Ballirano, P. & Cametti, G. (2012). *Microporous Mesoporous Mater.* **163**, 160-168.

Ballirano, P., Pacella, A., Cremisini, C., Nardi, E., Fantauzzi, M., Atzei, D., Rossi, A. & Cametti, G. (2015). *Microporous Mesoporous Mater.* **211**, 49-63.

Ballirano, P., Bloise, A., Gualtieri, A. F., Lezzerini, M., Pacella, A., Perchiazzi, N., Dogan, M. & Dogan, A.U. (2017). In A. F. Gualtieri, Ed., *Mineral Fibres: Crystal Chemistry, Chemical-Physical Properties, Biological Interaction and Toxicity. EMU Notes in Mineralogy*, London, **18**, 17-53.

Baris, Y. I., Sahin, A. A., Ozesmi, M., Kerse, I., Ozen, E., Kolacan, B., Altinörs, M. & Göktepeli, A. (1978). *Thorax*, **33**, 181-192.

Baris, Y. I., Saracci, R., Simonato, L., Skidmore, J.W. & Artvinli, M. (1981). *Lancet*, **2**, 984-987.

Bariş, B., Demir, A. U., Shehu, V., Karakoca, Y., Kisacik, G. & Bariş, Y. I. (1996). *J. Environ. Pathol. Toxicol. Oncol.* **15(2-4)**, 183-189

Belluso, E., Cavallo, A. & Halterman, D. (2017). In A.F. Gualtieri, Ed., Mineral Fibres: Crystal Chemistry, Chemical-Physical Properties, Biological Interaction and Toxicity. European Mineralogical Union-EMU Notes in Mineralogy, London, **18**, 65-109.

Bennett, J.M. & Grose, R.W. (1978). In L.B. Sand and F.A. Mumpton, Eds., *Natural Zeolites: Occurrence, Properties, Use*. Pergamon Press, Oxford, 77–83.

Bononi, A., Giorgi, C., Patergnani, S., Larson, D., Verbruggen, K., Tanji, M., Pellegrini, L., Signorato, V., Olivetto, F., Pastorino, S., Nasu, M., Napolitano, A., Gaudino, G., Morris, P., Sakamoto, G., Ferris, L. K., Danese, A., Raimondi, A., Tacchetti, C., Kuchay, S., Pass, H. I., Affar, E. B., Yang, H., Pinton, P. & Carbone, M. (2017). *Nature*, **546(7659)**, 549-553.

Burla, M. C., Caliandro, R., Carrozzini, B., Cascarano, G. L., Cuocci, C., Giacovazzo, C., Mallamo, M., Mazzone, A. & Polidori, G. (2015). *J. Appl. Cryst*. **48**, 306-309.

Cametti, G., Pacella, A., Mura, F., Rossi, M. & Ballirano, P. (2013). *Am. Mineral.* **98**, 2155-2163.

Carbone, M., Adusumilli, P. S., Alexander Jr, H. R., Baas, P., Bardelli, F., Bononi, A., Bueno, R., Felley-Bosco, E., Galateu-Salle, F., Jablons, D., Mansfield, A. S., Minaai, M., de Perrot, M., Pesavento, P., Rusch,

V., Severon, D. T., Taioli, E., Tsao, A., Woodard, G., Yang, H., Zauderer, G. & Pass, H.I. (2019). *Ca-Cancer J. Clin.* **69**, 402-429.

Carbone, M., Emri, S., Dogan, A. U., Steele, I., Tuncer, M., Pass, H. I. & Baris, Y. I. (2007). *Nat. Rev. Cancer* **7**, 147–154.

Carbone, M., Baris, Y. I., Bertino, P., Brass, B., Comertpay, S., Dogan, A. U., Gaudino, G., Jube, S., Kanodia, S., Partridge, C. R., Pass, H. I., Rivera, Z. S., Steele, I., Tuncer, M., Way, S., Yang, H. & Miller A. (2011). *PNAS* **108(33)**, 13618-13623.

Carbone, M. & Yang, H. (2012). *Clin. Cancer Res*. **18**, 598-604.

Carbone, M., Yang, H., Pass, H. I., Krausz, T., Testa, J. R. & Gaudino, G. (2013). *Nat. Rev. Cancer* **13**,153-159.

Carthew, P., Hill, R. J., Edwards, R. E. & Lee, P. N. (1992). *Hum. Exp. Toxicol*. **11(6)**, 530-534.

Churg, A. (1993). In G. D. Guthrie & B. T. Mossman, Eds., Health Effects of Mineral Dust. *Reviews in Mineralogy and Geochemistry*. Mineralogical Society of America, U.S.A. **28**, 409-426.

Clark, N. E., Verma, D. K. & Julian, J. A. (1995). *Ann. Occ. Hyg.* **39(1)**, 79-88.

Coelho, A. A. (2018). *J. Appl. Cryst.* **51**, 210-218.

Coffin, D. L., Cook, P. M. & Creason, J.P. (1992). *Inhal. Toxicol.* **4**, 273–300.

Coombs, D. C., Alberti, A., Armbruster, T., Artioli, G., Colella, C., Galli, E., Grice, J. D., liebau, F., Mandarino, J. A., Minato, H., Nickel, E. H., Passaglia, E., Peacor, D. R., Quartieri, S., Rinaldi, R., Ross, M., Sheppard, R. A., Tillmanns, E. & Vezzalini, G. (1997). *Canad. Mineral*. **35**, 1571–1606.

Deer, A., Howie, R., Wise, W. S. & Zussman, J. (2004). *Rock Forming Minerals. vol. 4B. Framework Silicates: Silica Minerals, Feldspathoids and the Zeolites*. The Geological Society, London.

Di Giuseppe, D., Scarfi, S., Alessandrini, A., Bassi, A. M., Mirata, S., Almonti, V., Ragazzini, G., Mescola, A., Filaferro, M., Avallone, R., Vitale, G., Scognamiglio, V. & Gualtieri, A. F. (2022). *Toxicology*, **466**, 153081.

Dogan, A. U. (2003). *Indoor Built Environ*. **12**, 337-342.

Dogan, M. (2012). *Scanning*, **34**, 37-42.

Dogan, A. U. & Dogan, M. (2008). *Environ. Geochem. Health* **30**, 355-366.

Dogan, A. U., Dogan, M. & Hoskins, J. A. (2008). *Environ. Geochem. Health* **30**, 367-381.

Donaldson, K., Murphy, F. A., Duffin, R. & Poland, C. A. (2010). *Part. Fibre Toxicol.* **7(1)**, 1-17.

Emri, S. A. (2017). *Ann. Transl. Med.* **5(11)**, 239-250.

Farrugia, L. J. (2012). *J. Appl. Cryst.* **45**, 849–854.

Gemmi M., Mugnaioli E., Gorelik T.E., Kolb U., Palatinus L., Boullay P., Hovmöller S. & Abrahams J.P. (2019). *ACS Cent. Sci*. **5**, 1315-1329.

Giacobbe, C., Di Giuseppe, D., Zoboli, A., Lassinantti Gualtieri, M., Bonasoni, P., Moliterni, A., Corriero, N., Altomare, A., Wright, J. & Gualtieri, A.F. (2021). *IUCrJ*, **8(1)**, 76-86.

Mertens, G. Madau, P., Durinck, D., Blanpain, B. & Elsen, J. (2007). *Cem. Concr. Res*. **37**, 1524-1530.

Gottardi, G. & Galli, E. (1985). *Natural Zeolites*, 409 p. Springer-Verlag, Heidelberg, Germany.

Gualtieri, A., Artioli, G., Passaglia, E., Bigi, S., Viani, A. & Hanson, J.C. (1998). *Am. Mineral*. **83**, 590-600.

Gualtieri, A. F., Bursi Gandolfi, N., Pollastri, S., Pollok, K. & Langenhorst, F. (2016). *Sci. Rep.* **6**, 37981-37992.

Gualtieri, A. F., Pollastri, S., Bursi Gandolfi, N. & Lassinantti Gualtieri, M. (2018). *Sci. Rep.* **8**, 7071-7083.

Gualtieri, A. F. (2018). *Toxicol. Appl. Pharmacol.* **361**, 89-98.

Gualtieri, A. F., Lusvardi, G., Zoboli, A., Di Giuseppe, D. & Lassinantti Gualtieri, M. (2019). *Environ. Res.* **171**, 550-557.

Guastoni, A., Dugnani, M., Pezzotta, F. & Bardelli, G. (2002). *Atti Soc. It. Sci. Nat. Museo Civ. St. Nat. Milano* **143**, 195-207.

Hill, R. J., Edwards, R. E. & Carthew, P. (1990). *J. Exp. Pathol.* **71**, 105–118.

IARC Working Group on the Evaluation of Carcinogenic Risks to Humans. (2012). Arsenic, metals, fibres, and dusts. IARC monographs on the evaluation of carcinogenic risks to humans, 100(PT C), 11.

Innes, E., Yiu, H. H. P., McLean, P., Brown, W. & Boyles, M. (2021). *Crit. Rev. Toxicol.* **51(3)**, 217-248.

Jones, J. B. (1968). *Acta Cryst.* B**24** 355 358.

Kawahara, A. & Curien, H. (1969). *Bulletin Societé Francaise Mineralogie Cristallographie*, **92**, 650–655.

Kerr, I. S., Gard, J. A., Barker, R. M. & Galabova, I.M. (1970). *Am. Mineral.* **55(3-4)**, 441-454.

Knops-Gerrits, P. P., De Vos, D. E., Feijen, E. J. & Jacobs, P. A. (1997). *Microporous Materials* **8(1-2)**, 3-17.

Kolb, U., Gorelik, T., Kübel, C., Otten, M. T. & Hubert, D. (2007). *Ultramicroscopy*, **107**, 507-513.

Kolb U., Mugnaioli E. & Gorelik T. E. (2011). *Cryst. Res. Technol.* **46 (6)**, 542-554.

Lawrence Bright, E., Giacobbe, C. & Wright, J. P. (2021). *J. Synchrotron Radiat.* **28(5)**, 1377-1385.

Lodish, H. F., Berk, A., Matsudaira, P., Kaiser, C. A., Krieger, M., Scott, M. P., Zipursky, L., Darnell, J. (1999). *Molecular cell biology*. MacMillan, pp. 1184.

Matassa, R., Familiari, G., Relucenti, M., Battaglione, E., Downing, C., Pacella, A., Cametti, G. & Ballirano, P. (2015). *Sci. Rep.* **5(1)**, 16757-16769.

Mattioli, M., Giordani, M., Arcangeli, P., Valentini, L., Boscardin, M., Pacella, A. & Ballirano, P. (2018). *Minerals*, **8(2)**, 69-85.

Metintaş, S., Batırel, H. F., Bayram, H., Yılmaz, Ü., Karadağ, M., Guntulu, Ak. & Metintaş M. (2017). *Int. J. Environ. Res. Public Health* , **14**, 1293-1306.

McCusker, L. B., Liebau, F. & Engelhardt, G. (2001). *Pure Appl. Chem*. **73**, 381-394.

Mugnaioli E. & Gemmi M. (2018). *Z. Kristallogr. - Cryst. Mater.* **233(3-4)**, 163-178.

Mugnaioli, E., Gorelik, T. & Kolb, U. (2009). *Ultramicroscopy*, **109**, 758-765.

Momma, K. & Izumi, F. (2011). *J. - Appl. Cryst.* **44(6),** 1272-1276.

NIMH (National Institute of Mental Health) (2018) ImageJ. https://imagej.nih.gov/ij/ (Accessed 19, September 2018).

Palatinus, L., Brázda, P., Jelínek, M., Hrdá, J., Steciuk, G. & Klementová, M. (2019). *Acta Cryst.* B**75(4)**, 512-522.

Pacella, A., Ballirano, P., Fantauzzi, M., Rossi, A., Nardi, E., Capitani, G., Arrizza, L. & Montereali, M. R. (2021). *Sci. Rep.* **11(1)**, 14249-14260.

Passaglia, E. (1970). *Am. Mineral.* **55**, 1278-1301.

Passaglia, E., Artioli, G. & Gualtieri, A. (1998). *Am. Mineral.* **83**, 577–589.

Passaglia, E. & Sheppard, R.A. (2001). *Rev. Mineral. Geochem.* **45(1)**, 69-116.

Rigaku (2015). CrysAlisPro Software System, Version 1.171.38.41. Rigaku Oxford Diffraction

Sebastien, P., Gaudichet, A., Bignon, J. & Baris, Y. I. (1981). *Lab. Invest.* **44**, 420–425.

Scapino, L., Zondag, H. A., Van Bael, J., Diriken, J. & Rindt, C. C. M. (2017). *Appl. Energy*, **190**, 920-948.

Sherry, H. S. (1979). *Clays Clay Miner.* **27(3)**, 231-237.

Schlenker, J. L., Pluth, J. J. & Smith, J.V. (1977). *Acta Cryst.* B**33**, 3265-3268.

Sheldrick, G.M. (2015). *Acta Cryst.* C**71(1)**, 3-8.

Simonato, L., Baris, R., Saracci, R., Skidmore, J. & Winkelmann, R. (1989). *IARC Sci. Publ.* **90**, 398-405.

Staples, L. W. & Gard, J. A. (1959). *Mineral. Mag.* **32**, 261–281.

Temel, A. & Gündoğdu, M. N. (1996). *Miner. Depos.* **31(6)**, 539-547.

Valdrè, G., Moro, D. & Ulian, G. (2018). In *IOP Conference Series: Materials Science and Engineering*, **304**, 1-11.

Van Gosen, B. S., Blitz, T.A., Plumlee, G. S., Meeker, G. P. & Pierson, M. P. (2013). *Environ. Geochem. Health*, **35(4)**, 419-430.

Van Koningsveld, H. (2007). *Compendium of zeolite framework types: building schemes and type characteristics*, 418 p. Elsevier, Amsterdam.

Vincent, R. & Midgley, P. A. (1994). *Ultramicroscopy*, **53**, 271-282.

Wagner, J. C., Skidmore, J. W., Hill, R. J. & Griffiths, D. M. (1985). *Br. J. Cancer*, **51**, 727–730.

Ward, J. W. (1972). *J. Catal.* **26**, 451-454

Westrip, S. P. (2010). *J. Appl. Cryst.* **43(4)**, 920-925.

Wopenka, B., Freeman, J. J. & Nikischer, T. (1998). *Appl. Spectrosc.* **52(1)**, 54-63.

Wylie, A. G. (2017). In *Asbestos and Mesothelioma*. Springer, Cham. 11-41.

Wright, J. P., Giacobbe, C. & Majkut, M. (2020). *Curr. Opin. Solid State Mater. Sci.* **24(2)**, 100818-100827.

Wright, J. P., Giacobbe, C. & Lawrence Bright, E. (2022). *Crystals*, **12(2)**, 255-263.